
Article:
Chakrabarty, S., Gleason, J.R., Han, Y. et al. (2024) Low frequency, 100–600 MHz, searches with axion cavity haloscopes. Physical Review D, 109. 042004. ISSN: 2470-0010

https://doi.org/10.1103/physrevd.109.042004

Low frequency, 100–600 MHz, searches with axion cavity haloscopes

S. Chakrabarty, J. R. Gleason, Y. Han, A. T. Hipp, M. Solano, P. Sikivie, N. S. Sullivan, and D. B. Tanner
University of Florida, Gainesville, Florida 32611, USA

M. Goryachev, E. Hartman, B. T. McAllister, A. Quiskamp, C. Thomson, and M. E. Tobar
University of Western Australia, Perth, Western Australia 6009, Australia

M. H. Awida, A. S. Chou, M. Hollister, S. Knirck, A. Sonnenschein, and W. Wester
Fermi National Accelerator Laboratory, Batavia, Illinois 60510, USA

T. Braine, M. Guzzetti, C. Hanretty, G. Leum, L. J Rosenberg, G. Rybka, and J. Sinnis
University of Washington, Seattle, Washington 98195, USA

John Clarke and I. Siddiqi
University of California, Berkeley, California 94720, USA

R. Khatiwada
Illinois Institute of Technology, Chicago, Illinois 60616, USA
and Fermi National Accelerator Laboratory, Batavia, Illinois 60510, USA

G. Carosi, N. Du, and N. Robertson
Lawrence Livermore National Laboratory, Livermore, California 94550, USA

L. D. Duffy
Los Alamos National Laboratory, Los Alamos, New Mexico 87545, USA

C. Boutan, N. S. Oblath, M. S. Taubman, J. Yang, and E. Lentz
Pacific Northwest National Laboratory, Richland, Washington 99354, USA

E. J. Daw and M. G. Perry
University of Sheffield, Sheffield S3 7RH, United Kingdom

C. Bartram
SLAC National Accelerator Laboratory, Menlo Park, California 94025, USA

J. H. Buckley, C. Gaikwad, J. Hoffman, and K. W. Murch
Washington University, St. Louis, Missouri 63130, USA

T. Nitta
International Center for Elementary Particle Physics, The University of Tokyo, Tokyo 113-0033, Japan

(Received 28 March 2023; accepted 19 December 2023; published 16 February 2024)

We investigate reentrant and dielectric loaded cavities for the purpose of extending the range of axion cavity haloscopes to lower masses, below the range where the Axion Dark Matter experiment (ADMX) has already searched. Reentrant and dielectric loaded cavities were simulated numerically to calculate and optimize their form factors and quality factors. A prototype reentrant cavity was built and its measured properties were compared with the simulations. We estimate the sensitivity of axion dark matter searches using reentrant and dielectric loaded cavities inserted in the existing ADMX magnet at the University of Washington and a large magnet being installed at Fermilab.

DOI: 10.1103/PhysRevD.109.042004

I. INTRODUCTION

Observations imply that a large fraction, of order 27%, of the energy density of the Universe is some unknown substance called "dark matter" [1]. Although we do not know the identity of the particles constituting dark matter, we know two essential properties: the dark matter particles must be collisionless and cold. "Cold" means that their primordial velocity dispersion is sufficiently small, less than about $10^{-8}c$ today, so that it may be set equal to zero as far as the formation of large scale structure and galactic halos is concerned. "Collisionless" means that the dark matter particles have, in first approximation, only gravitational interactions. Particles with the required properties are referred to as "cold dark matter." Axions produced in the early Universe by the process of "vacuum realignment" [2] have those properties [3]. Axions were originally proposed to solve the strong CP problem of the Standard Model of elementary particles [4,5], i.e., the puzzle of why the strong interactions conserve the discrete symmetries of parity P and charge conjugation times parity CP even though the Standard Model as a whole violates those symmetries. Therefore, the axion has a double motivation: it solves the strong CP and the dark matter problems simultaneously.

The axion is the quasi-Nambu-Goldstone boson associated with the spontaneous breaking of the $\mathrm{U_{PQ}}(1)$ quasisymmetry that Peccei and Quinn postulated to solve the strong CP problem. Its properties depend mainly on a single unknown parameter f_a, called the axion decay constant, of order the energy scale at which $\mathrm{U_{PQ}}(1)$ is spontaneously broken [6,7]. The axion mass and all axion couplings are inversely proportional to f_a. The axion mass is given by

$$m_a \simeq 6 \times 10^{-6}\ \mathrm{eV}\left(\frac{10^{12}\ \mathrm{GeV}}{f_a}\right). \tag{1.1}$$

The cold axion cosmological energy density is a decreasing function of increasing axion mass [2]. The axion mass for which the cold axion cosmological energy density equals that of dark matter is of order 10^{-5} eV, corresponding to f_a of order 10^{12} GeV, however with very large uncertainties [8]. A major source of uncertainty is whether cosmological inflation happens before or after the phase transition in which $\mathrm{U_{PQ}}(1)$ is spontaneously broken. In the postinflationary scenario; i.e., if the PQ phase transition occurs after inflation, then the cold axion cosmological energy density has contributions from axion string and axion wall decay in addition to the well-known contribution from vacuum realignment. Axion masses larger than 10^{-5} eV are favored in the postinflationary scenario because of these extra contributions.

In the preinflationary scenario; i.e., if the PQ phase transition occurs before inflation, then the cold axion cosmological energy density receives a contribution from vacuum realignment only. The vacuum realignment contribution is uncertain in the preinflationary scenario because it depends on the misalignment angle θ_1 of the axion field with respect to the minimum of its effective potential, at the start of the QCD phase transition. As a fraction of the critical energy density for closing the Universe, the cold axion energy density in the preinflationary scenario is of order [8]

$$\Omega_a \sim 0.15\left(\frac{f_a}{10^{12}\ \mathrm{GeV}}\right)^{\frac{7}{6}}\theta_1^2. \tag{1.2}$$

Since θ_1 is presumably a random number between $-\pi$ and $+\pi$, having the same value everywhere in the visible Universe because the axion field was homogenized during inflation [9], there is 10% probability that Ω_a is reduced by a factor 100, a 1% probability that it is reduced by a factor 10^4, and so on. For this reason, axion masses less than 10^{-5} eV are favored in the preinflationary scenario.

The PQ phase transition occurs at a temperature of order the axion decay constant $f_a \sim 10^{12}$ GeV. The reheat temperature at the end of inflation cannot be larger than the scale of inflation Λ_I and in many models it is of order or less than the Hubble rate H_I during inflation [10]. The nonobservation of tensor perturbations requires $H_I \lesssim 6 \times 10^{13}$ GeV [11] or, equivalently, $\Lambda_I < 1.6 \times 10^{16}$ GeV. So, there is limited room in (H_I, f_a) parameter space for the postinflationary scenario. On the other hand nothing forbids H_I and the reheat temperature from being very low compared to f_a. So there appears to be a lot of parameter space for the preinfationary scenario, suggesting that searches for axions with lower masses are well motivated.

A number of methods have been proposed to search for axion dark matter by direct detection on Earth. The topic is reviewed in Ref. [12]. The cavity haloscope method [13], the earliest method proposed, has obtained the best results so far. Experimental bounds have been obtained by the Axion Dark Matter eXperiment (ADMX) [14], HAYSTAC [15], CAPP [16], QUAX [17], RADES [18], ORGAN [19], and TASEH [20] collaborations. Additional experiments, such as MADMAX [21] and ALPHA [22], are in preparation. A cavity haloscope is an electromagnetic cavity permeated by a strong magnetic field and instrumented to detect small amounts of power inside the cavity. When one of the cavity's resonant frequencies equals the axion mass in natural units; i.e., when $\hbar\omega = m_a c^2$, where ω is the angular frequency of the resonant mode, a small amount of microwave power is deposited inside the cavity as a result of axion to photon conversion in the applied magnetic field.

The relevant interaction is

$$\mathcal{L}_{a\gamma\gamma} = -g_\gamma \frac{\alpha}{\pi}\frac{1}{f_a} a(x)\vec{E}(x)\cdot\vec{B}(x), \tag{1.3}$$

where α is the fine structure constant, $a(x)$, $\vec{E}(x)$, and $\vec{B}(x)$ are, respectively, the axion, electric, and magnetic fields,

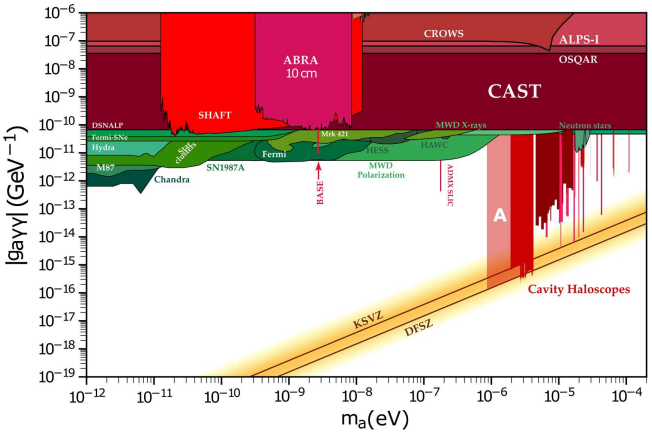

FIG. 1. Limits on the axion electromagnetic coupling $g_{a\gamma\gamma} \equiv g_\gamma \frac{\alpha}{\pi} \frac{1}{f_a}$ as a function of axion mass m_a, obtained by various axion searches. In addition, the light shaded area labeled A indicates the sensitivity, under assumptions spelled out in Sec. VI, of a search using a reentrant or dielectrically loaded cavity inserted in the "extended frequency range" (EFR) magnet that ADMX plans to operate at Fermilab. The figure was made by modifying Ciaran O'Hare's code [27] available at https://github.com/cajohare/AxionLimits.

and g_γ is a model-dependent factor of order one. In the context of the axion detection scheme described below, and all other axion cavity haloscopes, the magnetic field $\vec{B}(x)$ is dominated by the static external magnetic field $\vec{B}_0$ imposed to produce axion to photon conversion, whereas $\vec{E}(x)$ is the electric field of the produced photon. In the Kim-Shifman-Vainsthein-Zakharov model [6] $g_\gamma \simeq -1.01$, whereas $g_\gamma \simeq 0.32$ in the Dine-Fischler-Srednicki-Zhitnitskii (DFSZ) model [7]. Figure 1 shows the constraints that have been obtained so far on the electromagnetic coupling strength appearing in Eq. (1.3), $g_{a\gamma\gamma} \equiv g_\gamma \frac{\alpha}{\pi} \frac{1}{f_a}$, as a function of the axion mass. Using the cavity haloscope method, the ADMX has achieved sufficient sensitivity to find dark matter axions at the expected halo density and with DFSZ coupling, the weakest coupling of the two benchmark models mentioned [23–25]. So far, ADMX has searched in the 600 to 1050 MHz range. It plans to search at higher frequencies using multicavity arrays [26]. In this paper we explore methods to search lower frequencies, from approximately 100 to 600 MHz.

One approach to lower frequency axion dark matter detection is to replace the cavity with an LC circuit [28,29]. As with a haloscope cavity, the LC circuit is placed in a magnetic field. When its resonant frequency $\omega = 1/\sqrt{LC}$ equals the axion mass in natural units, the axion dark matter field drives a tiny current in the circuit. Haloscopes with LC circuits, instrumented with the highest signal to noise detectors available and placed in strong spatially extended magnetic fields, are expected to achieve the sensitivity required to detect axion dark matter on Earth. Several pilot projects have been carried out [30–32] and larger detectors are being planned [33]. An LC circuit is conveniently tuned by a variable capacitance. However the capacitance cannot be made arbitrarily small because a circuit always has some parasitic capacitance. Parasitic capacitance limits the highest frequency at which a large LC circuit may resonate [28]. For this reason, LC circuits large enough to be sensitive to axion dark matter are not expected to reach the 200–600 MHz frequency range, which is our main focus.

Instead, the approach we investigate here is to lower the resonant frequency of the cavity haloscope. This can be done of course by scaling up the physical size of the cavity, which indeed works very well assuming the magnetic field region is enlarged accordingly. However there are obvious limits as to how large the cavity and magnetic field region can be made. We therefore explore methods to lower the resonant frequency of the cavity without enlarging it. One approach is to fill the cavity with dielectric material, causing its resonant frequency to decrease as $1/\sqrt{\epsilon}$ where ϵ is the dielectric constant. The form factor C, which gives the strength of the coupling of the cavity mode to the axion dark matter field and which is defined in Eq. (2.3) below, decreases unfortunately as $\frac{1}{\epsilon}$ so that $C(f) \propto f^2$ where f is frequency. A second approach is to modify the cavity so as to make it "reentrant." Reentrant cavities are described in Sec. III A. Reentrant cavities for axion dark matter detection were proposed and discussed in Refs. [34,35], including the building and characterization of a prototype cavity. The form factor of a reentrant cavity also decreases qualitatively as $C(f) \propto f^2$. So it is not clear at the outset whether reentrant or dielectric loaded cavities are the better approach. The goal of this paper is to explore the two approaches systematically. In particular we consider several possible reentrant cavity designs and optimize them to achieve the highest possible form and quality factors. Whether one approach is better than the other ultimately depends on considerations such as the cost of low-loss dielectric materials and the lowest frequency that one wishes to attain with a given cavity.

The outline of our paper is as follows. In Sec. II, we give a general description of cavity haloscopes to prepare for the discussions that follow. In Sec. III, we report on numerical simulations of reentrant cavities. We consider several designs and optimize them for axion dark matter detection. In Sec. IV, we report on the measured properties of a prototype reentrant cavity that we built to validate the results of the numerical simulations. In Sec. V we report on numerical simulations of dielectric loaded cavities, evaluating their form and quality factors. In Sec. VI, we estimate the sensitivity that can be achieved using dielectric loaded and reentrant cavities inserted in the existing ADMX magnet at the University of Washington in Seattle and in a larger magnet that will be installed at Fermilab. Section VII summarizes our conclusions.

II. CAVITY HALOSCOPES

If axions constitute the dark matter halo of the Milky Way Galaxy, then we are immersed in a pseudoscalar field, the axion field, oscillating with angular frequency

$$\omega_a = \frac{1}{\hbar}E_a = \frac{1}{\hbar}\left(m_a c^2 + \frac{1}{2}m_a v^2\right) = \frac{1}{\hbar}m_a c^2[1+\mathcal{O}(10^{-6})], \tag{2.1}$$

where v is the speed of halo axions with respect to us. The ratio of their rest mass energy to their energy spread, called the "quality factor" Q_a of galactic halo axions, is expected to be of order 10^6 because the typical speed of halo dark matter is $10^{-3}c$. Note however that cold flows of axion dark matter are expected [36]. Such flows may have velocity dispersion much less than $10^{-3}c$ and correspondingly larger quality factors.

Henceforth, unless stated otherwise, we adopt units in which $\hbar = c = k_B = 1$.

A cavity haloscope searches for dark matter axions on Earth by attempting to convert them to microwave photons in an electromagnetic cavity permeated by a strong magnetic field [13]. The relevant coupling is given in Eq. (1.3). When the resonant frequency of cavity mode η equals the axion mass in natural units ($\omega_\eta = m_a$) and the quality factor Q_a of the axion signal is large compared to the loaded quality factor Q_η of the cavity in mode η, the power deposited into the cavity by the conversion process is in first approximation

$$P_\eta = g_{a\gamma\gamma}^2 \rho_a B_0^2 V C_\eta \frac{1}{m_a} Q_\eta, \tag{2.2}$$

where $g_{a\gamma\gamma} \equiv g_\gamma \frac{\alpha}{\pi}\frac{1}{f_a}$ is the coupling strength appearing in Eq. (1.3), ρ_a is the energy density of dark matter axions at the detector location, V is the volume of the cavity, B_0 is a nominal magnetic field strength inside the cavity, and

$$C_\eta = \frac{(\int_V d^3x \vec{B}_0(\vec{x})\cdot\vec{E}_\eta(\vec{x}))^2}{B_0^2 V \int_V d^3x \epsilon(\vec{x})\vec{E}_\eta(\vec{x})\cdot\vec{E}_\eta(\vec{x})}. \tag{2.3}$$

Here, $\vec{B}_0(\vec{x})$ is the actual static magnetic field inside the cavity, $\epsilon(\vec{x})$ is the dielectric constant, and the $\vec{E}_\eta(\vec{x})$ is the amplitude of the oscillating electric field in mode η. The form factor C_η expresses the coupling strength of mode η to galactic halo axions. Generally speaking, the cavity mode with the highest form factor is the lowest TM mode, with the longitudinal direction being that of the static magnetic field $\vec{B}_0$.

Equation (2.2) shows that the signal power is proportional to the loaded quality factor Q_η of the cavity when the axion signal falls exactly in the middle of the cavity bandwidth $B_\eta = f/Q_\eta$. Off resonance, the right-hand side (rhs) of Eq. (2.2) is multiplied by the Lorentzian response function characteristic of driven harmonic oscillators. Since the Lorentzian here has width B_η, the higher the quality factor the more narrow the frequency range over which the detector is sensitive at a given time. The overall figure of merit of a detector [12,37] is the rate at which it can search in frequency space with a given signal to noise ratio s/n. The search rate is given by

$$\frac{df}{dt} = \frac{1}{(s/n)^2}\left(\frac{P_\eta}{T_n}\right)^2 \frac{4}{9}\frac{Q_a}{Q_\eta}, \tag{2.4}$$

where T_n is the system noise temperature for detecting the microwave photons from axion conversion. Equation (2.4) assumes that the cavity bandwidth is much wider than the axion signal bandwidth ($Q_a \gg Q_\eta$) and that the loaded quality factor Q_η equals one third the unloaded quality factor. This latter condition maximizes the search rate for given unloaded quality factor [37]. Equations (2.2) and (2.4) show that the search rate is proportional to $C_\eta^2 Q_\eta$ when $Q_a \gg Q_\eta$ [37]. This is the quantity we wish to optimize. In practice, Q_η varies relatively little. So most of our focus is on optimizing C_η.

Both the reentrant cavity and the dielectric loaded cavity have form factors that decrease approximately as frequency squared as their resonant frequency f is lowered. For this reason, it is convenient when comparing designs to express their performance by the variable $\xi(f)$ defined by

$$C_\eta(f) = C_0\left(\frac{f}{f_0}\right)^2 \xi(f), \tag{2.5}$$

where f is the resonant frequency of the lowest TM mode, $C(f)$ is the form factor at that frequency, and C_0 and f_0 are the form factor and resonant frequency of the empty cavity in its TM_{010} mode. For the designs discussed here, the empty cavity is always a cylinder of length L and radius R, in which case $C_0 = 0.692$ and

$$f_0 = 574\ \text{MHz}\frac{0.2\ \text{m}}{R}. \tag{2.6}$$

To facilitate comparison between different designs, V in Eq. (2.3) is always be taken to be the volume of the empty cavity, $V = \pi R^2 L$.

Our goal is not only to evaluate the performance and optimize the design of reentrant and dielectric loaded cavities but also to present our results in such a way that they can be used in the widest possible set of contexts. Although C^2Q is the main figure of merit, we give separate results for C because C plays a more important role than Q and because Q affects the experiment in ways other than through C^2Q. We give our results concerning the form factor $C(f)$ in terms of $\xi(f)$ defined in Eq. (2.5) because this removes the rapid, approximately proportional to f^2,

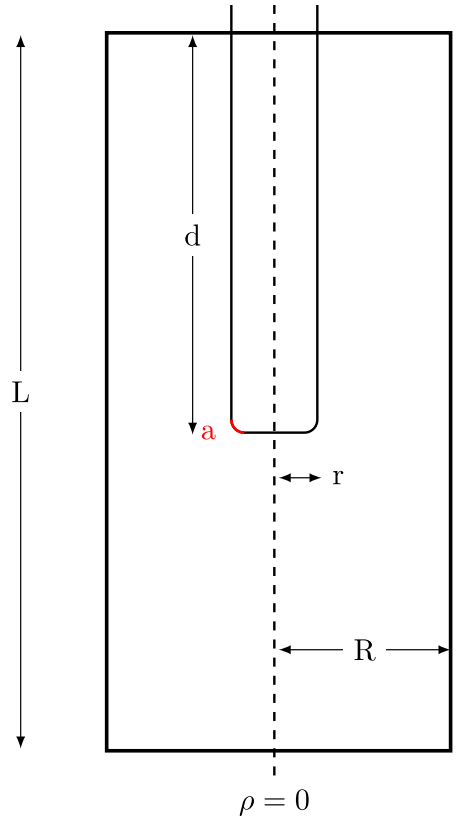

FIG. 2. Schematic drawing of a reentrant cavity with a simple movable post. The dashed line shows the cavity's symmetry axis. The figure defines the length L and radius R of the cavity, and the radius r and insertion depth d of the movable post. In red is shown the curvature radius a by which the edge of the end plate of the movable post is rounded.

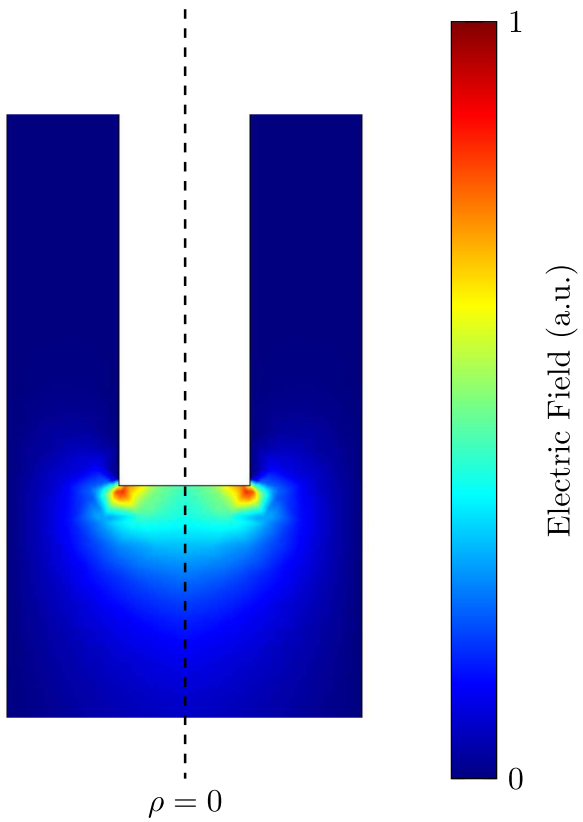

FIG. 3. E_z amplitude inside the reentrant cavity with a simple post for the case $L = 1.1$ m, $R = 0.325$ m, $r = R/2$, $d = 0.69$ m, and $a = 0$.

variation of C with f. We give our results concerning the quality factor Q in terms of $Q\delta/R$ because this removes the trivial dependence of Q on the skin depth δ and overall size of the cavity. The overall figure of merit is given as $\xi^2 Q\delta/R$ for those same reasons.

III. NUMERICAL SIMULATIONS OF REENTRANT CAVITIES

Figure 2 shows a tunable reentrant cavity consisting of a copper cylinder and a copper movable post that can be pushed in and out. The resonant frequency of the cavity decreases as the movable post is pushed in. All the reentrant cavity designs considered here are axially symmetric. The axial symmetry will be broken by the presence of the input and output ports that are necessary to couple out the axion signal and to characterize the cavity's properties. In this paper, we ignore the perturbations that the input and output ports introduce.

In the limit of axial symmetry the reentrant cavity mode of interest for axion dark matter detection has magnetic and electric fields of the form:

$$\vec{B}(\rho,z,\phi) = B(\rho,z)\hat{\phi},$$
$$\vec{E}(\rho,z,\phi) = \frac{i}{\omega}\left[\left(\frac{\partial B(\rho,z)}{\partial\rho} + \frac{B(\rho,z)}{\rho}\right)\hat{z} - \frac{\partial B(\rho,z)}{\partial z}\hat{\rho}\right], \quad (3.1)$$

where z, ρ, ϕ are cylindrical coordinates, and $\hat{z}, \hat{\rho}, \hat{\phi}$ are the corresponding unit vectors. $\hat{z}$ is in the direction both of the axis of axial symmetry of the cavity and of the static magnetic field $\vec{B}_0$. The mode with the largest form factor C is the lowest frequency mode of the type given in Eq. (3.1). It becomes the TM_{010} mode of the empty cylindrical cavity, when the post is removed.

In the remainder of this section, we report on reentrant cavity simulations aimed at identifying the designs of the movable post(s) that yield the largest form factors and quality factors for axion dark matter searches. For the simulations reported in this section and in Sec. V we used COMSOL software and a set of fortran codes that were written specifically for this project. The fortran codes can be found at https://www.phys.ufl.edu/ sikivie/simcav/. There was excellent agreement between the results obtained by the COMSOL and fortran codes.

A. Single movable post

Figure 2 shows a reentrant cavity tuned by a simple movable post. The figure defines the cavity length L and radius R, the radius r and insertion depth d of the movable post, and the rounding radius a of the edge of the movable post's end.

Figure 3 shows a map of the amplitude of the longitudinal component $E_z(z,\rho)$ of the electric field in the lowest TM mode of a reentrant cavity. The form factor C is proportional to the square of the volume integral of $E_z(z,\rho)$, see Eq. (2.3). Figure 3 shows that the main contribution to C comes from the region near the end of the post.

Figure 4 shows the resonant frequency f of the lowest TM mode as a function of the insertion depth d of the movable post for the case $L = 1$ m, $R = 0.2$ m, $r = 0.1$ m, and $a = 20$ mm. The figure also shows the resonant frequencies of the two lowest Transverse Electric (TE) modes, TE_{111}, and TE_{112}. There are no other modes within the tuning range. The reentrant cavity in its lowest Transverse Magnetic (TM) mode can be understood qualitatively as an LC circuit. The end of the movable post forms a capacitance with the bottom of the cavity. The oscillating current that charges and discharges this capacitance flows up (down) the post and down (up) the sides of the cavity. The circuit composed of the post and cavity sides has inductance. This inductance and the capacitance both increase as the post is inserted deeper, causing the resonant frequency to decrease. The resonant frequencies of the cavity TE modes do not change much as the post in inserted. Nominal design parameters do not support Transverse Electromagnetic (TEM) modes. As a result the lowest TM mode does not cross any other modes in the low frequency range of interest to us. This is an advantage of the reentrant cavity approach since the frequency intervals where mode crossings occur require special treatment in axion cavity haloscope searches.

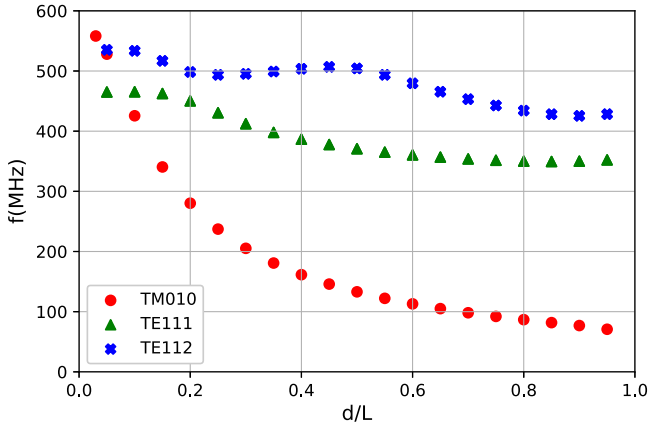

FIG. 4. Frequencies of a reentrant cavity's three lowest modes, TM_{010}, TE_{111}, and TE_{112}, as a function of insertion depth of a simple post for the case $L = 1$ m, $R = 0.2$ m, $r = 0.1$ m, and $a = 20$ mm. The TM_{010} mode is the mode used in an axion dark matter search.

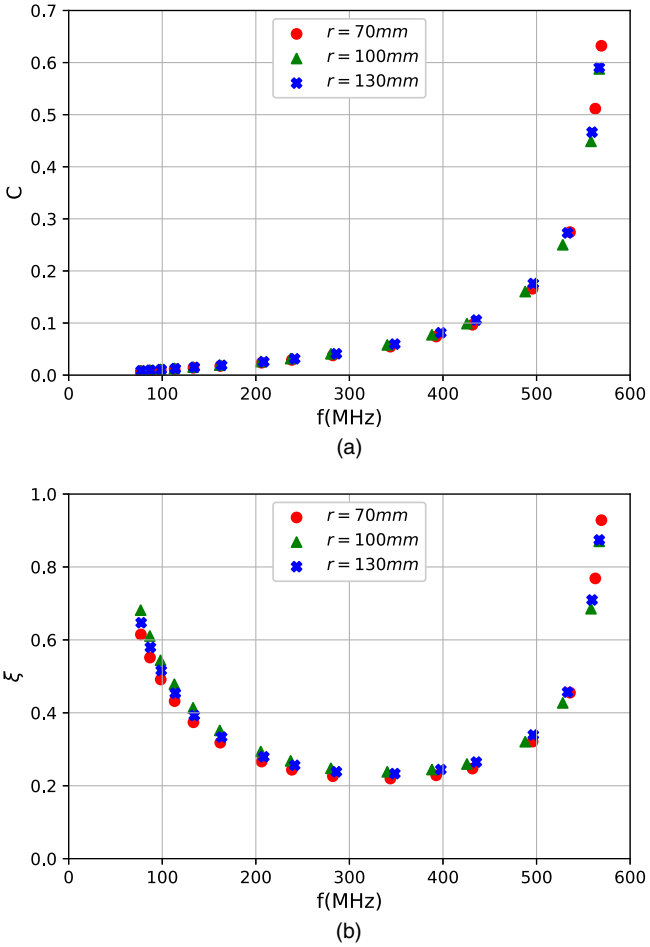

FIG. 5. (a) Form factor as a function of frequency for three values of the movable post radius r, inside a cavity of size $L = 1$ m, $R = 0.2$ m. (b) ξ as a function of frequency for the same data as in (a). At low frequencies, where the search is most challenging, the highest form factors are obtained when r is approximately $R/2$.

Figure 5(a) shows the form factor C as a function of frequency f for three different radii of the movable post. Qualitatively $C \propto f^2$. Figure 5(b) displays the same information in terms of the factor ξ defined in Eq. (2.5). The behavior shown is characteristic. By definition, ξ goes to one as $f \to f_0$. Below f_0, ξ decreases quickly to a minimum of order 0.25 for $f \sim 0.6 f_0$ and then increases again as f is lowered further. The minimum value depends on the length of the cavity as discussed below. At the lowest frequencies, where the search is most challenging because the form factor is lowest, the best performance in ξ is achieved by a post whose radius is about half the cavity radius.

Figure 6(a) shows the product of the quality factor Q times the skin depth δ as a function of frequency for several values of the movable post radius r. The skin depth is

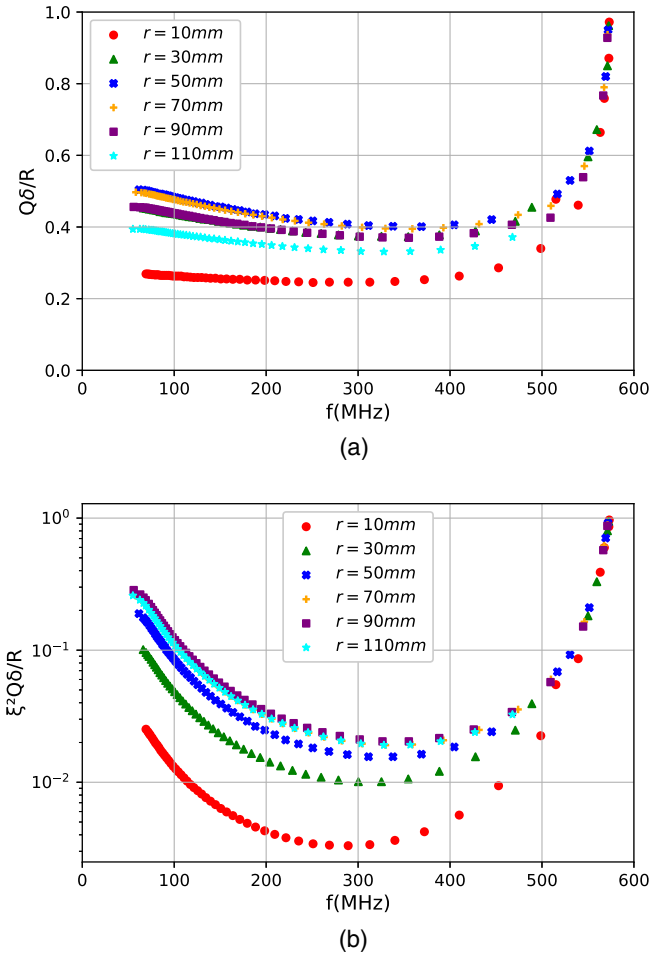

FIG. 6. (a) Product of the quality factor times the skin depth as a function of frequency for the case $L = 1$ m, $R = 0.2$ m, and several values of the movable post radius r. At low frequencies, where the search is most challenging, the highest quality factors are obtained when r is approximately $R/4$. (b) Figure of merit $\xi^2 Q\delta/R$ as a function of frequency for the case $L = 1$ m, $R = 0.2$ m, and several values of the movable post radius r, At low frequencies, where the search is most challenging, the highest figure of merit is obtained when $r \simeq 0.45R$.

assumed to be the same on all interior surfaces of the cavity. The quality factor is then equal to the product of $1/\delta$ times a factor which has dimension of length, is proportional to the overall size of the cavity and depends on its geometry. It is that factor that is plotted in the figure. The figure shows that the quality factor reaches a maximum when $r \simeq R/4$. Figure 6(b) shows $\xi^2 Q\delta/R$ as a function of frequency for several values of the movable post radius r. $\xi^2 Q\delta$ may be considered a figure of merit for a particular geometry since the search rate is proportional to $C^2 Q$, see Eq. (2.4). At the lowest frequencies, where the search is most challenging because the form factor C is smallest, $\xi^2 Q\delta$ is largest when $r \simeq 0.45R$.

Figure 7 shows the dependence of ξ and $Q\delta/R$ on the curvature radius a by which the edge of the post end cap is

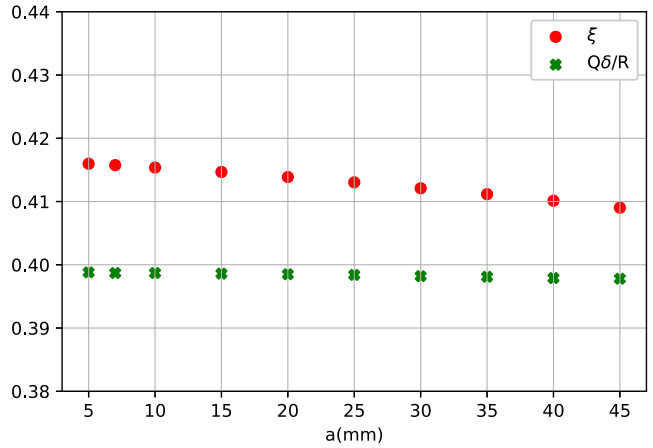

FIG. 7. ξ and $Q\delta/R$ as a function of the curvature radius a by which the edge of the movable post end cap is rounded off, for the case $L = 1$ m, $R = 0.2$ m, $r = 0.1$ m, and $d = 0.5$ m.

rounded. The figure, which has a suppressed origin, shows that there is very little such dependence. It appears that rounding off the edge of the post's end cap decreases both the form factor and the quality factor slightly in the case of a single post.

Figure 8 shows ξ and $Q\delta/R$ when the cavity's length L is decreased, from 1.0 to 0.55 m, while keeping fixed $R = 0.2$ m, $r = 0.1$ m, and $d = 0.5$ m. The figure shows that the product $L\xi$ is nearly constant over the L range shown. This is consistent with the fact that most of the contribution to the form factor comes from the region near the end of the movable post. In Fig. 3 the bottom third of the cavity is seen to contribute almost nothing to the form factor. It can therefore be removed without changing the sensitivity of the experiment. If we remove the bottom third, L and V are reduced by the factor $2/3$, but CV is

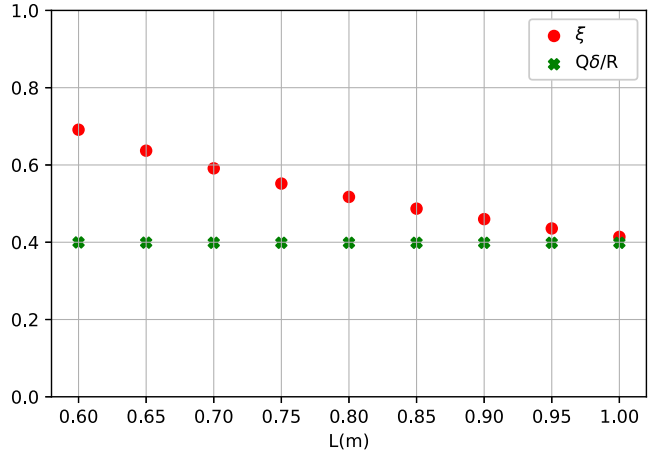

FIG. 8. Dependence of ξ and $Q\delta/R$ on the length of the cavity L. Note that the product of ξ and L and $Q\delta/R$ are very nearly constant, consistent with the statement that the part of the cavity away from the post can be removed without affecting the mode of interest.

approximately constant, as C and ξ are multiplied by $3/2$ approximately. The volume removed at no expense in sensitivity may be used for other purposes such as the placement of the mechanism that moves the tuning post. Alternatively, provided $L > 2d$, the ξ factor may be approximately doubled by installing a symmetrically placed post at the bottom of the cavity. In this case, to avoid mode localization in the bottom or top half of the cavity, the two oppositely placed posts should be identical and have equal insertion depths.

In this subsection, we reported on simulations of a reentrant cavity of length $L = 1$ m and radius $R = 0.2$ m, because that is the volume available inside the bore of the ADMX magnet at the University of Washington in Seattle. However, the results are applicable to practically any cylindrical cavity by exploiting (1) the fact that the dependence of the dimensionless quantities ξ and $Q\delta/R$ on the dimensionless variables L/R, r/R, and d/R is universal, and (2) the fact that ξL is approximately constant as long L as does not approach d.

We sought ways to improve the performance of the reentrant cavity by modifying the design of the movable post. We found many modifications that made the performance worse. One modification that improves performance is to add to the first post a second concentric post with smaller radius. This is discussed in Sec. III B. The performance can be improved still further by having a series of concentric posts with decreasing radii, as discussed in Sec. III C. One example of a modification that decreases performance is to add a disk at the end of the movable post, as illustrated in Fig. 9. In all cases simulated, the addition of a disk decreased the form factor, regardless of the thickness and radius of the disk.

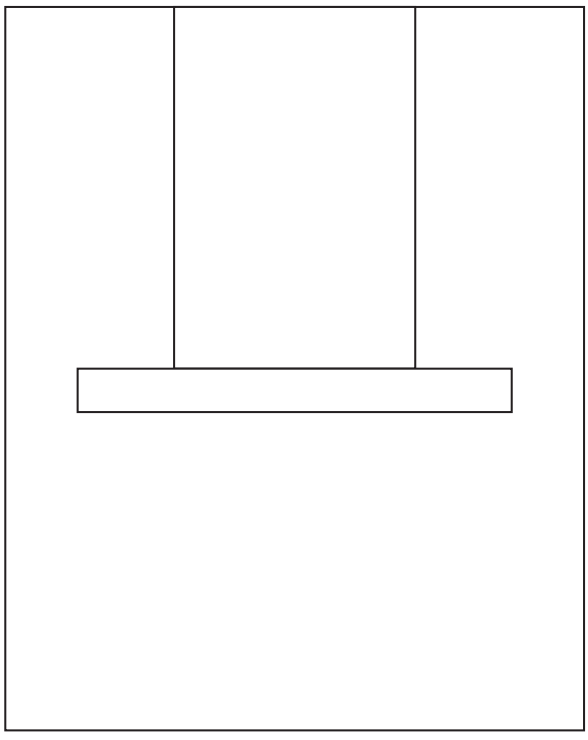

FIG. 9. Reentrant cavity with movable post and disk.

B. Fixed and movable posts

Figure 10 shows a reentrant cavity with a fixed post and a coaxial movable post that can slide through the fixed post. The figure defines the various dimensions of the posts, their lengths d_f and d_m, their radii r_f and r_m, and the radii a_f and a_m by which their ends are rounded. We simulated a cavity of length $L = 1$ m and radius $R = 0.325$ m. Such a cavity would fill the central volume of the EFR magnet that the ADMX collaboration plans to install and operate at Fermilab. The resonant frequency of the empty cavity in its lowest TM mode is $f_0 = 353$ MHz.

Our first step is to optimize the post dimensions so as to obtain the largest possible figure of merit $\xi^2 Q\delta$ at the lowest frequencies where we plan to operate, near 100 MHz. The optimization results do not depend sharply on the frequency where the optimization was done. The optimal values are $d_f = 0.176$ m, $r_f = 0.19$ m, $a_f = 70$ mm, $r_m = 0.12$ m, and $a_m \simeq 0$. The highest frequency that can be achieved is then 262 MHz, for $d_m = 0$. Higher frequencies, between 262 and 353 MHz, would be explored

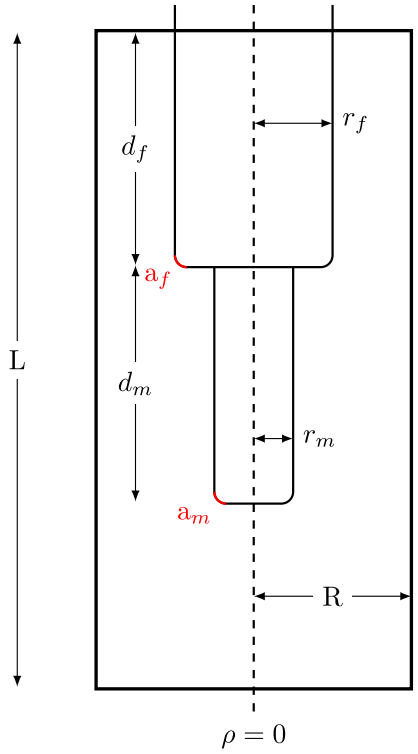

FIG. 10. Reentrant cavity with a fixed and a movable post. The figure defines the radii r_f and r_m of the fixed and of the movable posts, their insertion depths d_f and d_m, and the radii a_f and a_m by which their ends are rounded. The cavity is tuned by sliding the movable post through the fixed post.

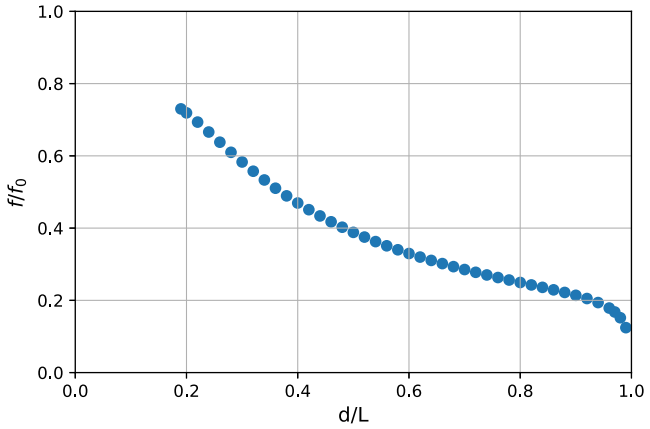

FIG. 11. Relative frequency f/f_0 versus relative insertion depth $d/L = (d_f + d_m)/L$ for the optimized reentrant cavity with a fixed and a movable post. f_0 is the frequency of the empty cavity. The cavity was optimized to achieve the highest figure of merit $\xi^2 Q\delta/R$ at $f/f_0 = 0.283$.

by using the cavity with a single post, as was described in the previous subsection.

Figure 11 shows the frequency of the optimized cavity as a function of the total insertion depth $d = d_f + d_m$. We plot the relative frequency f/f_0, where f_0 is the frequency of the empty cavity, versus d/L to emphasize that the relationships between dimensionless quantities are quasiuniversal. In the same spirit, Fig. 12 shows the dimensionless quantities ξ and $Q\delta/R$ as a function of f/f_0 for the optimized cavity, with $L/R = 0.308$.

It is useful to state how these results can be used for a cavity with a different radius, e.g., $R = 0.2$ m. Whatever the value of R, the optimal values of the post dimensions are $d_f \simeq 0.54R$, $r_f \simeq 0.58R$, $a_f \simeq 0.22R$, and $r_m \simeq 0.37R$, provided d does not approach L. If $R = 0.2$ m and $L = 0.308R = 0.615$ m, then Figs. 11 and 12 for the optimized cavity apply without change. If instead $R = 0.2$ m but $L = 1$ m, then Fig. 12 applies except that the ξ values should be rescaled using the fact that $\xi L =$ constant as long as L does not approach d. The comparison shows that the reentrant cavity with a fixed and a movable post performs somewhat better than the reentrant cavity with a simple movable post, improving the form factor typically by 10%. For example, at $f = 344$ MHz, the reentrant cavity with $R = 0.2$ m, $L = 1$ m and a simple post of radius $r = 0.1$ m, has $\xi = 0.235$. The same cavity at the same frequency but with optimized fixed and movable posts has $\xi = 0.264$.

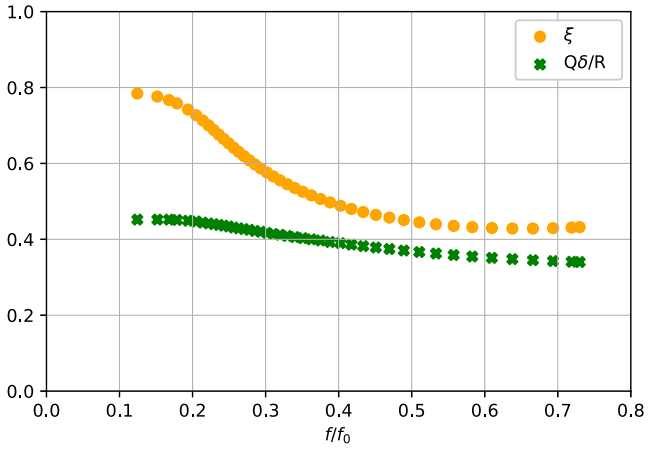

FIG. 12. ξ and $Q\delta/R$ versus relative frequency for the optimized reentrant cavity with a fixed and a movable post.

C. Telescopic post

To explore how much the form factor of a reentrant cavity can be improved further by inserting a post with several segments of successively smaller radii, we simulated the cavity depicted in Fig. 13 for the case $R = 0.325$ m and $L = 1.1$ m. Figure 14 shows the amplitude of the longitudinal component $E_z(z, \rho)$ of the electric field in the lowest TM mode of such a cavity. In the simulation, the post segment with the smallest radius is inserted first, followed by the other segments in order of increasing radii. The parameters r_i and r_o, defined in Fig. 13, and the number of segments n were varied to optimize ξ and $Q\delta$ at low frequencies. Figures 15 show the resulting ξ factor and $Q\delta/R$ as a function of frequency for a cavity with $n = 8$, $r_0 = 0.3$ m, and $r_i = 0.1$ m. The simulations show that the

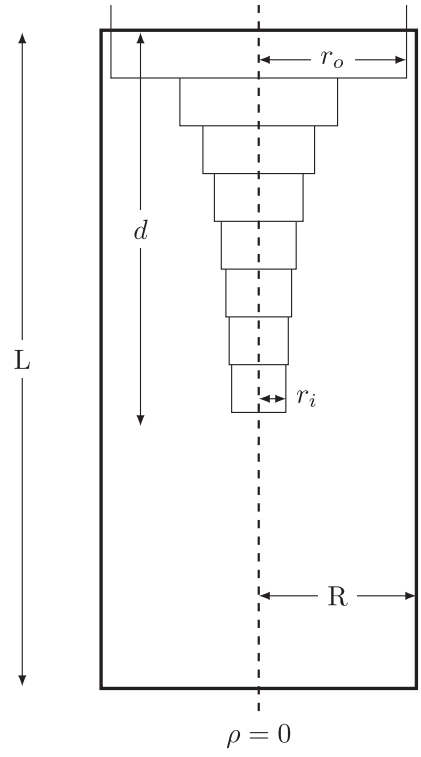

FIG. 13. Design of simulated cavity with telescopic post.

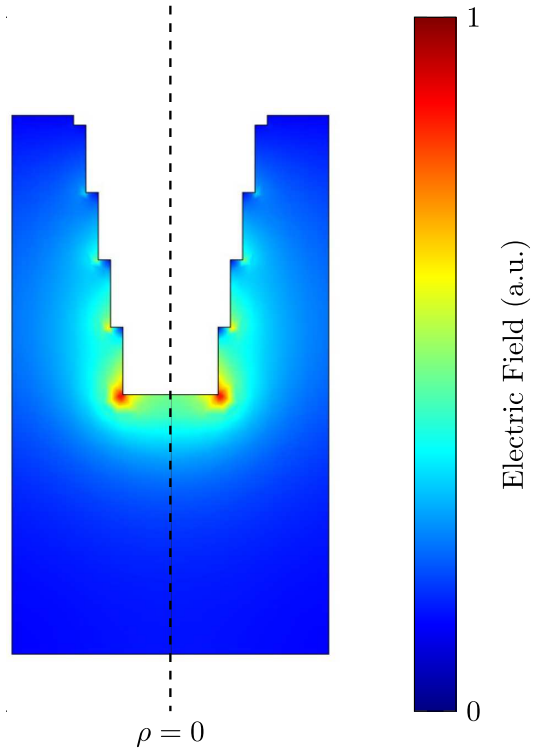

FIG. 14. E_z amplitude inside a reentrant cavity with a telescopic post.

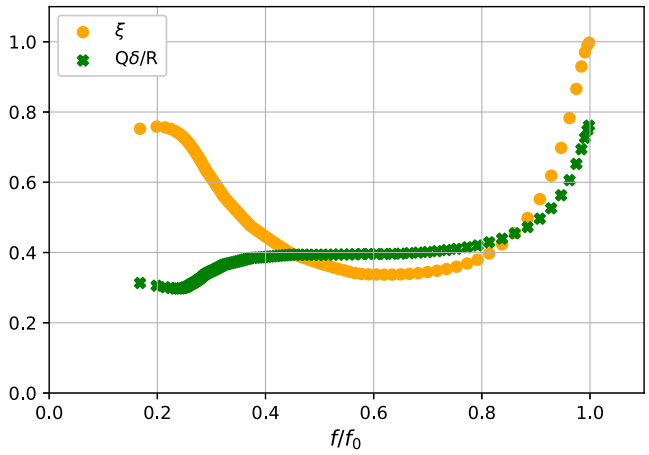

FIG. 15. ξ and $Q\delta/R$ versus frequency for the cavity with telescopic post.

telescopic post does improve the form factor near the lowest frequencies, where the search is most challenging.

In summary, we have in Sec. III presented numerical studies of the performance of axion haloscopes using reentrant cavities of three different designs. The main quantity determining performance is the form factor stated here in terms of its proxy $\xi(f)$, which was defined in Eq. (2.5). To facilitate comparison, Fig. 16 shows ξ versus frequency for the three designs in the same plot. The fixed and movable post design is perhaps most attractive because

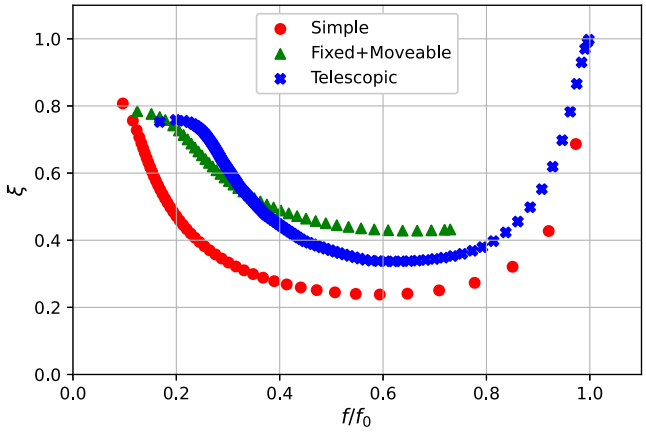

FIG. 16. ξ versus frequency for the three reentrant cavity designs that were simulated in detail.

it improves performance relative to a simple post while remaining relatively easy to build. In the next section we report on the performance of a prototype cavity with fixed and movable posts. When evaluating the sensitivity of contemplated low frequency axion halsocopes in Sec. VI we assume $\xi = 0.5$ throughout.

IV. PROTOTYPE REENTRANT CAVITY

A prototype reentrant cavity with fixed and movable posts was built and tested at the University of Florida. Figure 17 shows a schematic drawing of the cavity. It was built of OFHC copper and tested at room temperature. Its dimensions are $L = 0.381$ m, $R = 77$ mm, $d_f = 0.102$ m, $r_f = 54$ mm, $a_f = 6$ mm, $r_m = 27$ mm, and $a_m = 0$. The cavity is tuned by pushing the movable post in and out. The cavity has four probes to perform S11 and S12 measurements and study the best way to couple power in and out. The probes are coaxial rods of adjustable insertion depth. Each probe could be withdrawn entirely and each could be inserted at sufficient depth to achieve overcoupling. The measurements reported in Figs. 18 and 19 were done using the probes inserted through the fixed post, not those inserted through the top plate.

Figure 18 shows our measurements of its resonant frequency as a function of total insertion depth $d = d_f + d_m$ and the prediction from the numerical simulations. The agreement here is very good.

Figure 19 shows the quality factor as a function of frequency and the prediction from the simulations. The measured values are 15% to 40% lower than predicted. This may be due in part to an increase in the skin depth, compared to that of pure copper, caused by lack of cleanliness of the cavity's inner walls. However, even when a decrease in skin depth is allowed for, there is less than perfect agreement between theory and experiment in that Fig. 19 shows a dip in the measured values near 430 MHz, whereas there is no such dip in the predicted

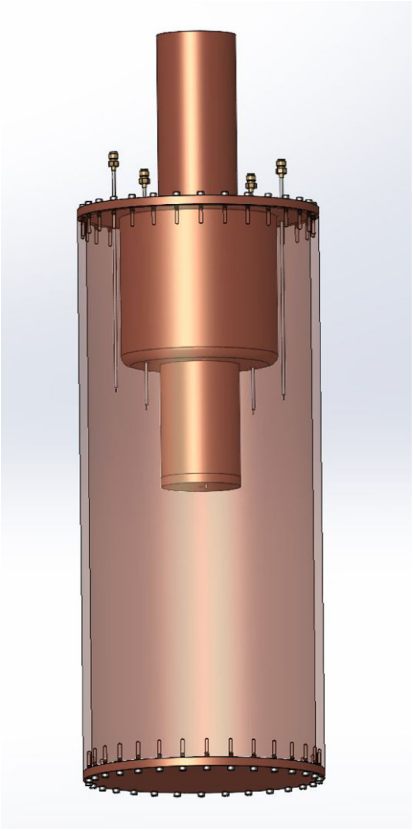

FIG. 17. Drawing of the prototype reentrant cavity described in Sec. IV.

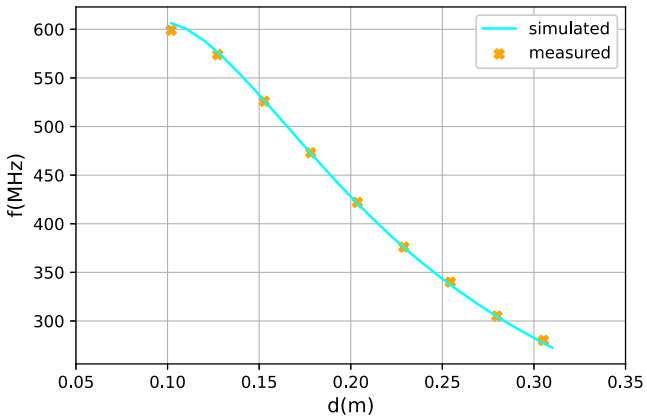

FIG. 18. Frequency versus total insertion depth $d = d_f + d_m$ of the prototype reentrant cavity.

values. We established that the dip is due to the mixing of the mode of interest, the cavity lowest TM mode, with a mode located outside the cavity. Indeed the dip can be made deeper and displaced in frequency by modifying the cavity environment. There may be leakage through the coaxial element formed by the movable and fixed posts in spite of the large capacitive coupling between the two posts. The issue will be investigated further.

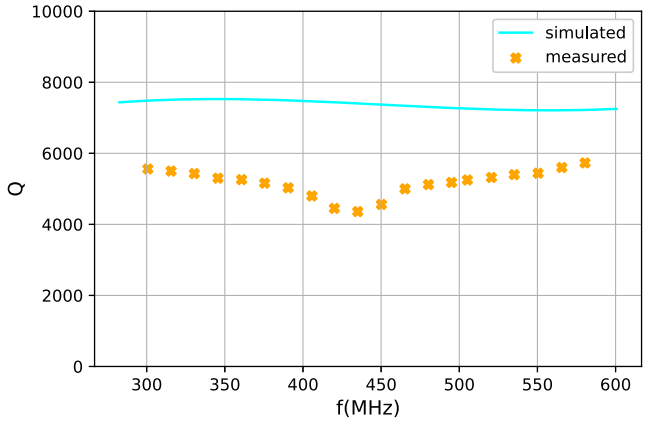

FIG. 19. Unloaded quality factor Q versus frequency of the prototype reentrant cavity.

V. NUMERICAL SIMULATIONS OF DIELECTRIC LOADED CAVITIES

In this section we investigate dielectric loading as a means to lower the resonant frequency of a cylindrical cavity in its lowest TM mode, keeping the cavity radius fixed. The cavity is tuned by moving a metallic rod sideways, a standard method used in cavity haloscopes. We assume that the dielectric material has properties similar to those of sapphire. Sapphire has a dielectric constant ranging from 9.3 to 11.5 depending on orientation and, for the purpose of cavity haloscopes, negligibly small dielectric losses at cryogenic temperatures [38]. Alumina (Al_2O_3) has the same chemical composition as sapphire and similar dielectric constant, but is more economical. High purity alumina has adequate dielectric losses for the purpose of axion haloscopes. In Ref. [39] the measured $\tan\delta$ is approximately 2×10^{-5} at room temperature. In our simulations, $\epsilon = 11.1$ and $\tan\delta = 10^{-7}$. Dielectric loading is a relatively straightforward concept. So there are fewer possibilities to explore here and less to report on than in Sec. III on reentrant cavities.

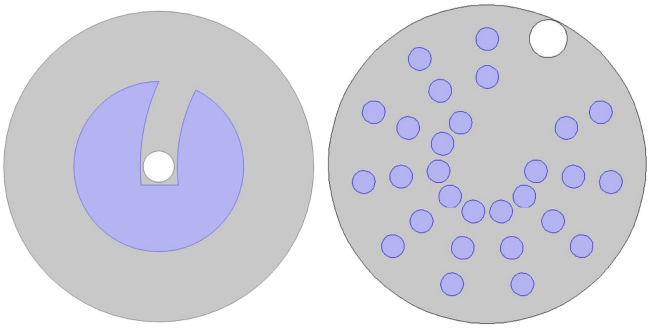

FIG. 20. Cross sectional view of dielectric loaded cavities. (a) Cavity loaded with a large ceramic cylinder machined to allow movement of a metallic tuning rod. The rod is at the cavity center. (b) Cavity loaded with 28 ceramic rods arranged to allow movement of a metallic tuning rod. The rod is at the cavity wall.

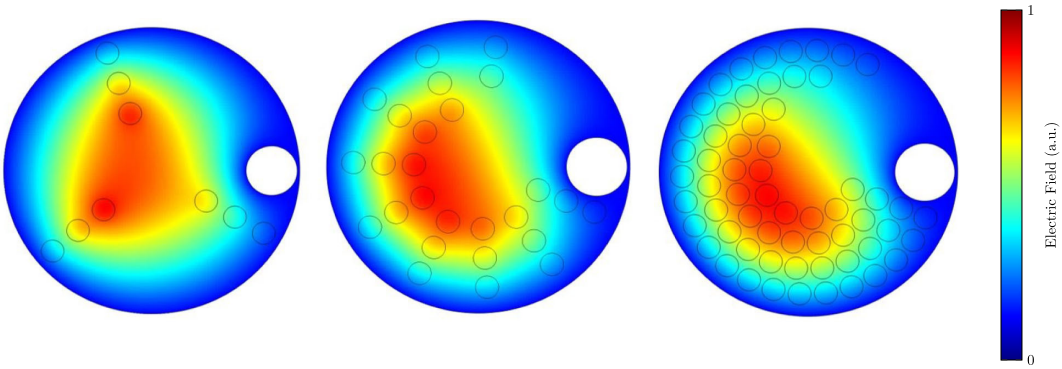

FIG. 21. Simulation of a cavity of radius 0.325 m loaded with different numbers of sapphire dielectric rods, each 12.5 mm in radius, and a metallic tuning rod. Dielectric loading enables the cavity to cover the frequency range 165–370 MHz. (a) 286.43 MHz resonant mode with 9 rods, (b) 216.73 MHz resonant mode with 26 rods, and (c) 164.59 MHz resonant mode with 61 rods.

Dielectric inserts have been introduced into cavity haloscopes to increase the quality factor at high frequencies, near 10 GHz [40,41]. The purpose of our dielectric inserts is instead to lower the frequency to near 200 MHz. The quality factor will not be improved thereby, so $Q_a \gg Q_\eta$ will remain true as in previous ADMX searches.

Figure 20 depicts cross sectional views of two possible designs. The cavity in (a) has a large ceramic cylinder machined to allow the movement of the metallic tuning rod. The cavity in (b) has instead many ceramic rods of small radius. Using many small rods is simpler and more feasible in terms of fabrication.

A cavity of radius $R = 0.325$ m and length $L = 1$ m was simulated in three configurations, with $N = 9$, 26, and 61 dielectric rods, as shown in Fig. 21. In all cases, the dielectric rods have radius 12.5 mm, the metallic tuning rod has radius 56 mm for $N = 9$, and 65 mm for $N = 26$ and 61. The frequency range 165–370 MHz is covered without gaps by the three configurations. The cavity with a metallic tuning rod of radius 50 mm and no dielectric rods covers 370–525 MHz.

Figure 22 shows ξ and $Q\delta/R$ as a function of frequency for the three dielectric loaded configurations. Unlike reentrant cavities, dielectric loaded cavities are prone to mode crossings. In this particular example, each configuration has one major mode crossing where the form factor dips.

VI. SENSITIVITY ESTIMATES

In this section, we estimate the downward reach in frequency of reentrant and dielectric loaded cavities installed in the magnet presently in use by ADMX at the University of Washington (UW) in Seattle and in the EFR magnet that ADMX plans to install and operate at Fermilab. For the UW magnet, we take $L = 1$ m, $R = 0.2$ m, and $B_0 = 7.5$ T. For the EFR magnet $L = 1$ m, $R = 0.325$ m, and $B_0 = 9$ T.

We assume here that $\xi \simeq 0.5$ will be achieved by the low frequency cavities whether they use the reentrant or the dielectric loaded design, In view of our simulations [see Figs. 5(b), 12, 15, and 21(a)], $\xi = 0.5$ is a conservative value at the lowest frequencies where the search is most challenging in all cases. $\xi = 0.5$ is equivalent to

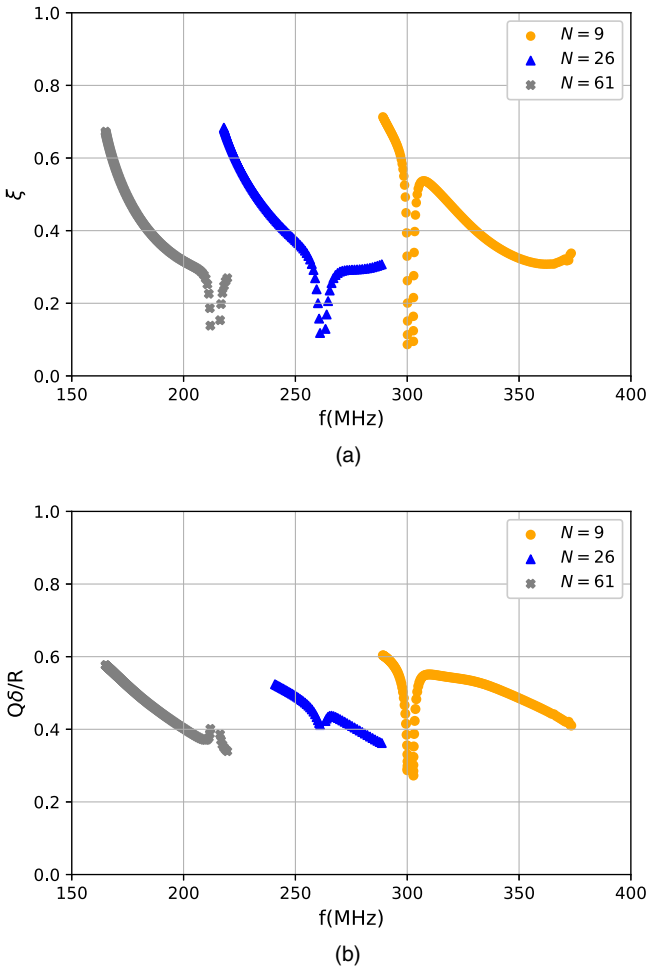

FIG. 22. (a) ξ and (b) $Q\delta/R$ versus frequency for the different dielectric loading configurations described in Fig. 20. The dip in each curve is due to mode crossing, and mixing, with a TE mode.

$C(f) = 0.35(f/f_0)^2$. Furthermore, for both the reentrant and dielectric loaded cavities, we assume that the quality factor is of the same order as the quality factors achieved in the ADMX cavities in the past.

We make two alternative assumptions about the density and energy dispersion of the local dark matter axion density. Assumption A is that the axion energy density is $\rho_a = 450$ MeV/cc and $Q_a = 10^6$. Assumption A is what the ADMX collaboration has consistently used in the past to derive limits on the coupling $g = g_{a\gamma\gamma}$ from its observations. Assumption B is the prediction of the galactic halo model described in Ref. [42]. Observational evidence is claimed for that model in Refs. [42,43]. The model predicts the existence on Earth of a cold flow, called the "big flow," with energy density estimated to be not less than 6 GeV/cc [43] and velocity dispersion not more than 70 m/s [44]. This latter upper limit implies a quality factor for the axion signal from the big flow not less than 0.5×10^{10}. For assumption B, we set $\rho_a = 6$ GeV/cc and $Q_a = 0.5 \times 10^{10}$.

Combining Eqs. (2.2) and (2.4) we have

$$s/n = \frac{2}{3}\left(\frac{g}{g_{\mathrm{DFSZ}}}\right)^2 g_{\mathrm{DFSZ}}^2 \rho_a B_0^2 V C \frac{1}{m_a}\frac{1}{T_{\mathrm{n}}}\sqrt{\frac{Q_\eta Q_a}{f\frac{d\ln f}{dt}}}. \tag{6.1}$$

Since we ask how low in frequency a given detector may go with sufficient signal to noise ratio to find or rule out axions under stated conditions, we are interested in the frequency dependence on the rhs of Eq. (6.1). We assume that the search rate over a logarithmic frequency scale $\frac{d\ln f}{dt}$ is fixed at some reasonable value, similar to what ADMX has achieved in the past. We assume that $\xi = 0.5$, a reasonable value for searches at the lowest envisaged frequencies in view of our simulations. Hence $C(f) \simeq 0.35(f/f_0)^2$. We assume that the total noise temperature T_{n} is dominated by the physical temperature of the cavity, in which case T_{n} is frequency independent. This is discussed further in the next paragraph. Since $g_{\mathrm{DFSZ}} \propto m_a \propto f$, and $Q_\eta \propto f^{\frac{1}{3}}$ in the anomalous skin depth regime appropriate for the cryogenic temperatures at which we plan to operate the cavity, we have

$$s/n \propto \left(\frac{g}{g_{\mathrm{DFSZ}}}\right)^2 \rho_a B_0^2 V \sqrt{Q_a} f^{\frac{8}{3}}, \tag{6.2}$$

where we show explicitly those factors that depend on the magnet used (UW or EFR) and on the assumptions on the local axion dark matter density (A or B). Equation (6.2) shows that searches with reentrant or dielectric loaded cavities become sharply more challenging as the frequency is lowered, mainly because of the worsening form factor and the decreasing coupling. It is our goal to estimate the lowest frequency $f_\star$ at which the search is feasible under stated conditions, with the understanding that the search is then comparatively easy at frequencies larger than of order $f_\star$.

The total noise temperature T_{n} is the sum of the physical temperature T_{phys} of the cavity and the system noise temperature T_{det} of the detector of microwave photons produced by axion to photon conversion. Our assumption is that T_{det} is of order T_{phys} or less. At present the ADMX detector at UW achieves $T_{\mathrm{phys}} \simeq 150$ mK using a dilution refrigerator. The so-called "quantum limit" on the noise temperature of receivers is $\hbar\omega/k_{\mathrm{B}} = 29$ mK $(\frac{f}{600\ \mathrm{MHz}})$. John Clake and collaborators [45] developed quantum limited SQUID detectors for ADMX axion searches in the 600–800 MHz range [23,46]. Our assumption regarding T_{n} is satisfied if near quantum limited receivers are developed and used in the 100–600 MHz range.

When estimating the sensitivity under the various stated assumptions we use as a benchmark the ADMX search reported in Ref. [23]. It excluded DFSZ coupled axions in the frequency range 645–678 MHz using the UW magnet under assumption A on the local axion density. The cavity was tuned upwards from the empty cavity resonant frequency $f_0 = 574$ MHz using a copper tuning rod. In that search $C \simeq 0.4$ and $T_{\mathrm{n}} \simeq 300$ mK. The signal to noise ratio s/n was approximately 4 because of the desirability of having of order one candidate signal per cavity tune from statistical fluctuations in the noise and the fact that the noise is Gaussian distributed for the medium frequency resolution appropriate in a search under assumption A.

A. Using the UW magnet

Under assumption A (Maxwell-Boltzmann) and the above stated conditions, Eq. (6.2) implies

$$s/n \simeq 4\left(\frac{g}{g_{\mathrm{DFSZ}}}\right)^2\left(\frac{f}{574\ \mathrm{MHz}}\right)^{\frac{8}{3}}. \tag{6.3}$$

Since $s/n \simeq 4$ is necessary under assumption A, the search is sensitive to a coupling of the axion to two photons

$$g = g_{\mathrm{DFSZ}}\left(\frac{574\ \mathrm{MHz}}{f}\right)^{\frac{4}{3}}, \tag{6.4}$$

i.e., $f_*|_{UW,A} = 574$ MHz. Although sensitivity to DFSZ coupling is lost, the search is still sensitive to Kim-Shifman-Vainsthein-Zakharov coupling over a wide frequency range. It is also sensitive to many models of dark matter in the form of axionlike particles, as well as to QCD axions in theories where the coupling to two photons is enhanced for cosmological reasons, such as axion initial kinetic misalignment [47,48], or particle physics reasons such as in the photophilic hadronic axion model of Ref. [49].

Under assumption B (big flow), the rhs of Eq. (6.2) is multiplied by $(6/0.45)\sqrt{5 \times 10^3}$ compared to the search

under assumption A in view of the increases in ρ_a and Q_a. Hence

$$s/n \simeq 3.8 \times 10^3 \left(\frac{g}{g_{\mathrm{DFSZ}}}\right)^2 \left(\frac{f}{574\ \mathrm{MHz}}\right)^{\frac{8}{3}}. \quad (6.5)$$

On the other hand, a high resolution search that fully exploits assumption B requires $s/n \simeq 14$ because the noise is exponentially distributed in such a search and there are of order 10^5 frequency bins per cavity tune in which candidate signals may occur [50]. Hence the lowest frequency at which sensitivity to DFSZ coupling can be achieved under the stated conditions is

$$f_\star|_{\mathrm{UW,B}} = \left(\frac{14}{3.8 \times 10^3}\right)^{\frac{3}{8}} 574\ \mathrm{MHz} = 70\ \mathrm{MHz}. \quad (6.6)$$

B. Using the EFR magnet

Compared to the UW magnet $B_0^2 V$ is multiplied by $(\frac{9}{7.5})^2(\frac{32.5}{20})^2 = 3.8$. Moreover, f_0 is lowered to $\frac{20}{32.5}574\,\mathrm{MHz} = 353\,\mathrm{MHz}$. Under assumption A (Maxwell-Boltzmann), Eq. (6.4) is replaced by

$$g = g_{\mathrm{DFSZ}} \frac{1}{\sqrt{3.8}} \left(\frac{353\ \mathrm{MHz}}{f}\right)^{\frac{4}{3}}. \quad (6.7)$$

The lowest frequency at which sensitivity to DFSZ coupling can be achieved under the stated conditions is then

$$f_\star|_{\mathrm{EFR,A}} = 214\ \mathrm{MHz}. \quad (6.8)$$

The reach of a reentrant cavity haloscope installed in the EFR magnet, under assumption A (Maxwell-Boltzmann), is shown in Fig. 1.

Under assumption B (big flow), the rhs of Eq. (6.5) is multiplied by the factor 3.8 in addition to the replacement 574 MHz → 353 MHz for the resonant frequency of the empty cavity. This yields

$$f_\star|_{\mathrm{EFR,B}} = 26\ \mathrm{MHz}. \quad (6.9)$$

VII. SUMMARY

We argued that there is comparatively more room in parameter space for inflation to occur after the PQ phase transition than before that transition. This motivates axion dark matter searches at frequencies lower than where ADMX has already searched. The resonant frequency of axion haloscopes can be lowered by increasing the overall size of the cavity. Although attractive in several respects, this approach is limited by the size of available magnets in which to insert the cavity. In this paper we explored instead the possibility of lowering the resonant frequency by making the cavity reentrant or by loading it with dielectric material.

We simulated reentrant and dieletric loaded cavities numerically to compute their form factors and quality factors. We explored several designs of the movable post that is inserted in a reentrant cavity to tune it, and optimized the post dimensions. The tuning posts with the highest figure of merit have radii that decrease with depth into the cavity. Our results are presented in a way which can be easily applied to cylindrical cavities of arbitrary dimensions.

We built a tunable reentrant cavity and compared its measured properties with the simulations. The agreement was excellent in the plot of resonant frequency versus tuning post insertion depth. In the plot of the quality factor versus frequency, the measured values were between 15% to 40% lower than the predicted ones. The origin of this discrepancy is under further investigation.

For both the reentrant cavity and the dielectric loaded cavity the form factor C decreases with decreasing frequency qualitatively as f^2, so an axion search becomes progressively more challenging as the frequency is lowered. We estimated the lowest frequency f_* at which a search with DFSZ sensitivity can be carried out using the magnet presently used by ADMX at the University of Washington and the larger EFR magnet that ADMX plans to operate at Fermilab. The estimates are given by Eqs. (6.6), (6.8), and (6.9) for two alternative assumptions about the local dark matter density.

ACKNOWLEDGMENTS

This work was supported by the U.S. Department of Energy through Grants No. DE-SC0022148, No. DE-SC0009800, No. DESC0009723, No. DE-SC0010296, No. DE-SC0010280, No. DE-SC0011665, No. DEFG02-97ER41029, No. DEFG02-96ER40956, No. DEAC52-07NA27344, No. DEC03-76SF00098, and No. DESC0017987. Fermilab is a U.S. Department of Energy, Office of Science, HEP User Facility. Fermilab is managed byFermi Research Alliance, LLC (FRA), acting under Contract No. DE-AC02-07CH11359. Additional support was provided by the Heising-Simons Foundation and by the Lawrence Livermore National Laboratory, LLNL Release No. LLNL-JRNL-846819. Pacific Northwest National Laboratory is a multiprogram national laboratory operated for the U.S. DOE by Battelle Memorial Institute under Contract No. DE-AC05-76RL01830. U. W. A. was funded by the ARC Centre of Excellence for Engineered Quantum Systems, Grant No. CE170100009, and Dark Matter Particle Physics, Grant No. CE200100008. B. M. is funded by the Forrest Research Foundation. C. B. acknowledges support from the Panofsky Fellowship at SLAC.

[1] *Particle Dark Matter*, edited by G. Bertone (Cambridge University Press, Cambridge, England, 2010).
[2] J. Preskill, M. Wise, and F. Wilczek, Phys. Lett. B **120B**, 127 (1983); L. Abbott and P. Sikivie, Phys. Lett. **120B**, 133 (1983); M. Dine and W. Fischler, Phys. Lett. **120B**, 137 (1983).
[3] J. Ipser and P. Sikivie, Phys. Rev. Lett. **50**, 925 (1983).
[4] R. D. Peccei and H. Quinn, Phys. Rev. Lett. **38**, 1440 (1977); Phys. Rev. D **16**, 1791 (1977).
[5] S. Weinberg, Phys. Rev. Lett. **40**, 223 (1978); F. Wilczek, Phys. Rev. Lett. **40**, 279 (1978).
[6] J. Kim, Phys. Rev. Lett. **43**, 103 (1979); M. A. Shifman, A. I. Vainshtein, and V. I. Zakharov, Nucl. Phys. **B166**, 493 (1980).
[7] M. Dine, W. Fischler, and M. Srednicki, Phys. Lett. **104B**, 199 (1981); A. Zhitnitskii, Sov. J. Nucl. **31**, 260 (1980).
[8] Reviews of axion cosmology include: P. Sikivie, Lect. Notes Phys. **741**, 083513 (2005); D. J. E. Marsh, Phys. Rep. **643**, 1 (2016).
[9] S.-Y. Pi, Phys. Rev. Lett. **52**, 1725 (1984).
[10] S. Weinberg, *Cosmology* (Oxford University Press, New York, 2008).
[11] Y. Akrami *et al.* (Planck Collaboration), Astron. Astrophys. **641**, A10 (2020).
[12] P. Sikivie, Rev. Mod. Phys. **93**, 015004 (2021).
[13] P. Sikivie, Phys. Rev. Lett. **51**, 1415 (1983); **52**, 695(E) (1984); **52**, 2988 (1985); **36**, 974(E) (1987).
[14] C. Bartram *et al.* (the ADMX Collaboration), Phys. Rev. Lett. **127**, 261803 (2021), and references therein.
[15] K. M. Backes *et al.* (The HAYSTAC Collaboration), Nature (London) **590**, 7845 (2021), and references therein.
[16] A. K. Yi *et al.* (The CAPP Collaboration), Phys. Rev. Lett. **130**, 071002 (2023), and references therein.
[17] D. Alesini *et al.* (The QUAX Collaboration), Phys. Rev. D **103**, 102004 (2021), and references therein.
[18] A. Alvarez Melcon *et al.* (The RADES Collaboration), J. High Energy Phys. 21 (2020) 075.
[19] B. McAllister, G. Flower, E. N. Ivanov, M. Goryachev, J. Bourhill, and M. E. Tobar (The ORGAN Collaboration), Phys. Dark Universe **18**, 67 (2017).
[20] H. Chang *et al.* (The TASEH Collaboration), Phys. Rev. Lett. **129**, 111802 (2022).
[21] B. Majorovits, EPJ Web Conf. **282**, 01008 (2023).
[22] A. J. Millar *et al.* (The ALPHA Collaboration), Phys. Rev. D **107**, 055013 (2023).
[23] N. Du *et al.*, Phys. Rev. Lett. **120**, 151301 (2018).
[24] T. Braine *et al.*, Phys. Rev. Lett. **124**, 101303 (2020); C. Bartram *et al.*, Phys. Rev. D **103**, 032002 (2021).
[25] C. Bartram *et al.*, Phys. Rev. Lett. **127**, 261803 (2021).
[26] J. Yang, and G. Rybka, Springer Proc. Phys. **245**, 53 (2020).
[27] C. O'Hare, Axion Limits (2022), https://cajohare.github.io/AxionLimits/.
[28] P. Sikivie, N. Sullivan, and D. Tanner, Phys. Rev. Lett. **112**, 131301 (2014).
[29] Y. Kahn, B. R. Safdi, and J. Thaler, Phys. Rev. Lett. **117**, 141801 (2016).
[30] J. L. Ouellet *et al.*, Phys. Rev. Lett. **122**, 121801 (2019); Phys. Rev. D **99**, 052012 (2019).
[31] N. Crisosto, P. Sikivie, N. S. Sullivan, D. B. Tanner, J. Yang, and G. Rybka, Phys. Rev. Lett. **124**, 241101 (2020).
[32] C. P. Salemi *et al.*, Phys. Rev. Lett. **127**, 081801 (2021).
[33] L. Brouwer *et al.*, arXiv:2204.13781; A. AlShirawi *et al.*, arXiv:2302.14084.
[34] B. T. McAllister, S. R. Parker, and M. E. Tobar, Phys. Rev. D **94**, 042001 (2016).
[35] B. T. McAllister, Y. Shen, G. Flower, S. R. Parker, and M. E. Tobar, J. Appl. Phys. **122**, 144501 (2017).
[36] P. Sikivie and J. R. Ipser, Phys. Lett. B **291**, 288 (1992).
[37] C. Hagmann, P. Sikivie, N. Sullivan, D. B. Tanner, and S.-I. Cho, Rev. Sci. Instrum. **61**, 1076 (1990).
[38] J. Krupka, K. Derzakowski, M. Tobar, J. Hartnett, and R. G Geyer, Meas. Sci. Technol. **10**, 387 (1999).
[39] N. M. Alford and S. J. Penn, J. Appl. Phys. **80**, 5895 (1996).
[40] D. Alesini *et al.* (The QUAX Collaboration), Nucl. Instrum. Methods Phys. Res., Sect. A **985**, 164641 (2021).
[41] S. Bae, S. Youn, and J. Jeong, Phys. Rev. D **107**, 015012 (2023).
[42] L. D. Duffy and P. Sikivie, Phys. Rev. D **78**, 063508 (2008).
[43] S. S. Chakrabarty, Y. Han, A. H. Gonzalez, and P. Sikivie, Phys. Dark Universe **33**, 100838 (2021).
[44] N. Banik and P. Sikivie, Phys. Rev. D **93**, 103509 (2016).
[45] M. Mück, M.-O. André, J. Clarke, Jost. Gail, and C. Heiden, Appl. Phys. Lett. **72**, 2885 (1998).
[46] S. J. Asztalos *et al.*, Phys. Rev. Lett. **104**, 041301 (2010).
[47] R. T. Co, L. J. Hall, and K. Harigaya, Phys. Rev. Lett. **120**, 211602 (2018); **124**, 251802 (2020).
[48] C. Eroncel, R. Sato, G. Servant, and P. Sørensen, J. Cosmol. Astropart. Phys. 10 (2022) 053.
[49] A. V. Sokolev and A. Ringwald, J. High Energy Phys. 06 (2021) 123.
[50] L. D. Duffy, P. Sikivie, D. B. Tanner, S. Asztalos, C. Hagmann, D. Kinion, L. J Rosenberg, K. van Bibber, D. Yu, and R. F. Bradley, Phys. Rev. Lett. **95**, 091304 (2005); Phys. Rev. D **74**, 012006 (2006); J. Hoskins *et al.*, Phys. Rev. D **84**, 121302 (2011).